Adaptive Wireless Power Transfer System With Relay Transmission and Communication

Jia-Jing Kao, Chun-Liang Lin, *Senior Member, IEEE*, and Jamie Yang

***Abstract*—Wireless power transmission (WPT) systems have been increasingly utilized for wireless charging of electric vehicles. However, most research efforts or commercial products only address wireless power transmission but not wireless data communication. In addition, limitation of the transmission range is always a gap obstructing its popularity. Accordingly, this article presents a novel WPT scheme incorporating both relay transmission and magnetic field data communication. For power transmission, a resonant inverter with pulsewidth modulation was developed using relay coils to induce longer distance alternating current. For data transmission, a magnetic field communication system based on impedance changes and not reliant on extra radio frequency links was realized. Fuzzy compensation was used to stabilize the transmission of both power and data to counter changes in mutual inductance between coils. Phase-shift keying was utilized to generate digital signals for data transmission. Our experimental prototype was tested and verified to simultaneously transmit power and data in compliance with SAE TIR J2954 specifications using real-world experiments.**

***Index Terms*—Fuzzy control, magnetic field communication, wireless charge, wireless power transmission (WPT) relay transmission.**

I. Introduction

WIRELESS power transmission (WPT), wireless energy transmission, or electromagnetic power transfer is a method of electrical energy transmission through electromagnetic induction without using wires as a physical link [1]. It is useful to various power electrical devices while interconnecting wires are not allowed, impossible or inconvenient.

In recent years, WPT-based charging technology has become more mature than ever because of the increasing popularity of mobile devices and electric vehicles. Various systems using WPT technology are now ubiquitous, including bidirectional WPT [2], mobile wireless charging [3], vehicle dynamic charging [4], and electricity and data transmission systems [5]. WPT systems can be classified into various categories such as the following:

Manuscript received 3 April 2022; revised 20 June 2022, 8 August 2022, and 22 September 2022; accepted 17 October 2022. Date of publication 31 October 2022; date of current version 26 December 2022. This work was supported by the Ministry of Science and Technology, Taiwan, under Grant MOST 110-2634-F-005-006. Recommended for publication by Associate Editor M. Vitelli. *(Corresponding author: Chun-Liang Lin.)*

The authors are with the Department of Electrical Engineering, Smart Sustainable New Agriculture Research Center, National Chung Hsing University, Taichung 40227, Taiwan (e-mail: kao19681968@yahoo.com.tw; chunlin@dragon.nchu.edu.tw; g110064154@mail.nchu.edu.tw).

Color versions of one or more figures in this article are available at https://doi.org/10.1109/TPEL.2022.3218368.

Digital Object Identifier 10.1109/TPEL.2022.3218368

1) inductive power transmission (IPT) power is transferred between coils of wire by a magnetic field [6];
2) magnetic resonant power transfer (MRPT) power is transferred by magnetic fields between two resonant circuits where the two are tuned to resonate at the same resonant frequency to increase coupling and power transfer [7];
3) high-resonant WPT-high quality factor resonators are utilized to enable efficient energy transfer at lower coupling rates for greater power transfer distances [8].

For IPT, ordinary inductive coupling can achieve high efficiency only when the coils are close together, usually adjacent. However, in most modern inductive systems, magnetic resonant WPT is considered, in which the efficiency is increased by adopting resonant circuits to achieve high efficiencies at greater distances.

The Society of Automotive Engineers (SAE) announced the first version of the wireless charging specification SAE TIR *J2954* in 2016 [9]. Three standards have been specified for the output power and transmission distance of a system. The current version of the standard has addressed nonbidirectional grid-to-vehicle (G_2V) charging, which is the charging method used for stationary vehicles. In the future, bidirectional power transfer (G_2V or V_2G), dynamic applications, and embedded installations may be considered and evaluated.

The aforementioned WPT functions do not involve or address communication. In addition, most theoretical studies focusing on the WPT systems did not address compensation of coil misalignment and data transmission. In the works [10], [11], [12], [13], [14], various approaches have been developed for single directional or bidirectional IPT schemes. In [15], this article investigated the efficiency of a MRPT WPT in conducting medium and found out an optimal operational frequency. In [16], a WPT system, that can adapt to changing air-gap distances, was demonstrated; however, the system could not transmit power and data simultaneously. In [17], a wireless power and data transfer via an inductive link based on frequency division multiplexing was proposed. However, the system works with two operating frequencies, which may result in relatively high cost. The WPT systems proposed in [18], [19], and [20] can execute power relay transmission with various configurations such as introducing a relay coil, however, data transmission was not the focus and the configuration was not general. In [20], an optimization method for WPT system with the use of a repeater is presented to enhance transferred power. However, the scenario limited to one repeater. The researchers in [13] and [21] have proposed WPT systems with a coil misalignment detection mechanism,

TABLE I
COMPARISON OF RECENT WPT RELATED APPROACHES

	WPT method	Power transfer mode	Data communication	Modulation type	Compliance with SAE standard	Coil misalignment compensation	Mechanism for increasing transmission distance
[10, 12]	IPT	Bidirectional	-	-	Y	-	-
[11]	IPT	Bidirectional	-	-	-	-	-
[12]	IPT	Bidirectional	-	-	NA	-	-
[14]	IPT	Single directional	-	-	-	-	-
[15]	MRPT	Single directional	-	-	-	-	-
[16]	IPT	Single directional	-	-	-	Y	-
[17]	MRPT	Single directional	Y	NA	-	-	-
[18-20]	IPT	Single directional	-	-	-	-	One repeater
[22]	IPT	Single directional	-	-	Y	Y	-
[23]	IPT	Bidirectional	Y	BPSK	Y	Y	-
Proposed system	MRPT	Bidirectional	Y	MPSK	Y	Y	Expandable repeaters

however, clear data transmission volume was not presented. In [22], three transmission coils were used to compensate for coil misalignment, however, this design also excluded data transmission.

Various recent academic developments of WPT approaches are as follows: the IPT approach [10], [11], [12], [13], [14], [16], [18], [19], [20], [22], [23] and the MPRT approach [15], [17]; the single directional power transfer [14], [15], [16], [17], [18], [19], [20], [22] and the bidirectional power transfer [10], [11], [12], [13], [23]; the design with communication capability [17], [23] where the approach of [23] was equipped with the binary phase shift keying (BPSK); the designs presented in [10], [13], [22], and [23] were complied with SAE standard; the approaches considering coil misalignment compensation were [16], [22], [23]; the approaches covering a repeater to increase transmission distance were depicted in [18], [19], and [20]. Most research efforts cited only address WPT with no wireless data communication included. This is because, in practical environments, vehicle status can mostly be monitored on the web page via the grid side connecting a cloud server. It allows users to monitor vehicle charging status (and more) via mobile networks. However, when there is in the absence of radio frequency (RF) links (such as the underground parking lots), the vehicle would not be able to communicate with the grid side. Moreover, an additional communication link is necessary for the frequency control scheme, and stability issues such as frequency interference may occur. In addition, limitation of the power transmission range is always a gap obstructing its popularity.

In our previous work [23], a WPT system for use in electric vehicles (EVs) was demonstrated to successfully achieve simultaneous wireless power and data transmission without additional RF links. The system adopts magnetic induction technology that might limit its transmission capability in terms of transmission distance, allowable coil misalignment, and air gap. Additionally, the amplitude-shift keying modulation used in the system is susceptible to noise interference. The present approach presents an updated approach by introducing magnetic resonance for power transfer and relay coils to induce longer power transferring range.

The contributions are summarized below by providing solutions to mitigate drawbacks of the existing results in the follows.

1) Developing the architecture of expandable relay coils to enhance power transfer flexibility so as to accommodate EVs with various chassis heights.
2) Establishing a synchronous grid–vehicle power and data transmission scheme to waive the need of extra RF links.
3) Proposing fuzzy control to reduce quality drops in efficiency and communication engendered by significant coil misalignment.
4) Introducing an exclusive encoding and decoding mechanism to ensure data communication accuracy in situations involving vehicle parking deviation.
5) Employing the multiple phase shift keying (MPSK) technique to improve utilization rate of the frequency band.

Tabled comparison of the proposed approach with the existing ones is given in Table I, which summarizes distinguishing advantages in terms of power transfer enhancement, communication function, and compensation of the proposed approaches. Real-world experiments have been conducted in this article task to validate the proposed design.

II. RELAY TRANSMISSION AND DRIVER

WPT is a new type of power transmission method that achieves no wire contact between the power supply and the load under the electromagnetic effect or energy exchange. Magnetic induction wireless transmission technology mainly uses the principle of electromagnetic induction to transmit electrical power. It can be simply expressed that the iron core of a transformer is changed to an air gap. Magnetic resonance wireless transmission generates a magnetic field through a resonant circuit to achieve the transfer of electricity. The system architecture is similar to magnetic induction, but the coils and circuits on both sides must be set at a specific frequency to achieve resonance.

A. Analysis of Relay Transmission Circuit

The proposed strategy for charging EVs with n repeaters is presented in Fig. 1. The schematic diagram for the entire system to comply with different chassis heights of EVs is illustrated in Fig. 2. The mutual inductance M between a pair of coils can be

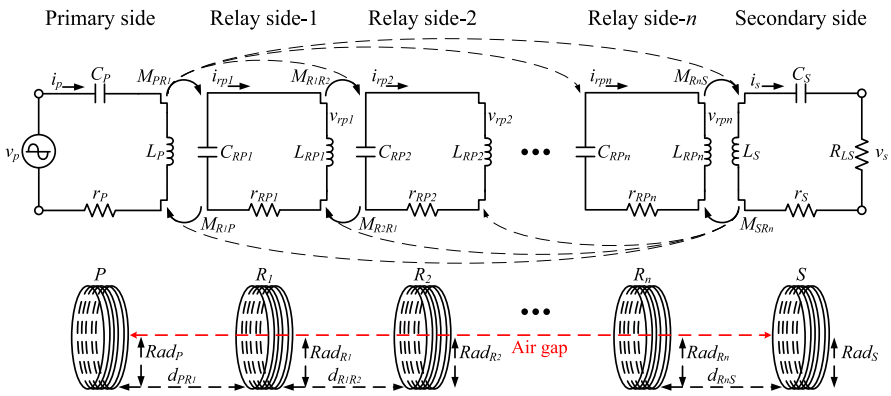

Fig. 1. Schematic of the WPT system with n repeaters.

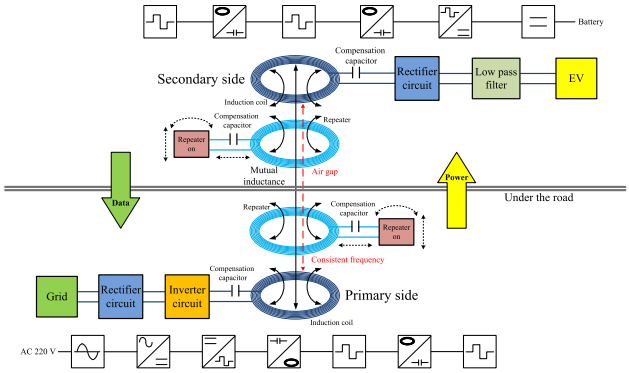

Fig. 2. Proposed strategy for charging EVs with various chassis heights.

represented as follows:

$$M_{PR_1} \approx M_{R_1R_2} \cdots \approx M_{R_nS} \gg M_{PS} \tag{1}$$

where M_{ij} is the mutual inductance between coils i and j $(i, j = P, R_1, \ldots, R_n, S; i \neq j)$. The ω domain voltage loop equation is expressed as

$$\begin{aligned}
v_p = &\left[r_P + j\left(\omega L_P - \tfrac{1}{\omega C_P}\right)\right] i_p + j\omega M_{PR_1} i_{rp1} \\
&+ \cdots + j\omega M_{PR_n} i_{rpn} + j\omega M_{PS} i_s, \\
0 = &\; j\omega M_{R_1P} i_p + \left[r_{RP1} + j\left(\omega L_{RP1} - \tfrac{1}{\omega C_{RP1}}\right)\right] \\
&\times i_{rp1} + \cdots + j\omega M_{R_1R_n} i_{rpn} + j\omega M_{R_1S} i_s, \\
&\vdots \\
0 = &\; j\omega M_{R_nP} i_p + j\omega M_{R_nR_1} i_{rp1} + \cdots \\
&+ \left[r_{RPn} + j\left(\omega L_{RPn} - \tfrac{1}{\omega C_{RPn}}\right)\right] i_{rpn} + j\omega M_{R_nS} i_s, \\
0 = &\; j\omega M_{SP} i_p + j\omega M_{SR_1} i_{rp1} + \cdots + j\omega M_{SR_n} i_{rpn} \\
&+ \left[r_S + R_{LS} + j\left(\omega L_S - \tfrac{1}{\omega C_S}\right)\right] i_s
\end{aligned} \tag{2}$$

in which L_{RPn} and C_{RPn} are the coil inductance and capacitance of relay side-n, respectively. Moreover, r_{RPn} and i_{rpn} are the internal resistance and the current flowing through L_{RPn}, respectively, and. The power transfer efficiency (PTE) η of the system can be derived as follows:

$$\eta = \left[\frac{i_s^2 R_{LS}}{i_p^2 r_P + i_{rp1}^2 r_{RP1} + \cdots + i_s^2 (r_S + R_{LS})}\right] \cdot 100\%. \tag{3}$$

When the system is operating at the resonant frequency, the frequency f, and angular frequency ω are known to be $f = \frac{1}{2\pi\sqrt{LC}}$ and $\omega = \frac{1}{\sqrt{LC}}$, respectively.

Assume that the system has the same resonance frequency; accordingly, η can be expressed as

$$\eta \equiv f(L, M, r, R_{LS}) \tag{4}$$

where $L \equiv L_P, L_{RP1}, \cdots, L_S, M \equiv M_{R_1R_2}, \cdots, M_{R_nS}$, and $r \equiv r_P, r_{RP1}, \cdots, r_S$, or equivalently

$$\eta \equiv f(L, Rad, C, r, R_{LS}) \tag{5}$$

where $Rad \equiv Rad_P, Rad_{R_1}, \cdots, Rad_S$ and $C \equiv C_P, C_{\mathrm{RP1}}, \cdots, C_S$ using Maxwell's equations.

The preceding formula shows that the coil radius and the distance between coils affect the PTE of the system [24]. Therefore, to simplify the scenario, in our WPT system design, the distance *d* between the repeaters is equidistant, and the radius *Rad* of each coil is identical. It can be seen from the abovementioned formula that the radius of the coil and the distance between coils will affect the power transfer efficiency of the system. Without loss of generality, inductive coils with the same size will be used and placed with equal distances from each other in the subsequent development.

B. Full-Bridge Inverter

Fig. 3 shows the proposed symmetrical driver architecture with relay transmission (under G_2V). The main circuit includes a resonant inverter, resonant repeaters, full-wave rectifier, modulation circuit, measurement circuits, and synchronization circuits. The microcontroller realizes power drive, fuzzy compensation, signal modulation, and data encoding/decoding. In addition, the fuzzy button connected to the microcontrollers provides real-time coil misalignment compensation.

In this architecture, ac_1 generates vp_{bus} through the rectifier on the primary side. V_{GS1}/V_{GS4} and V_{GS2}/V_{GS3} represent the

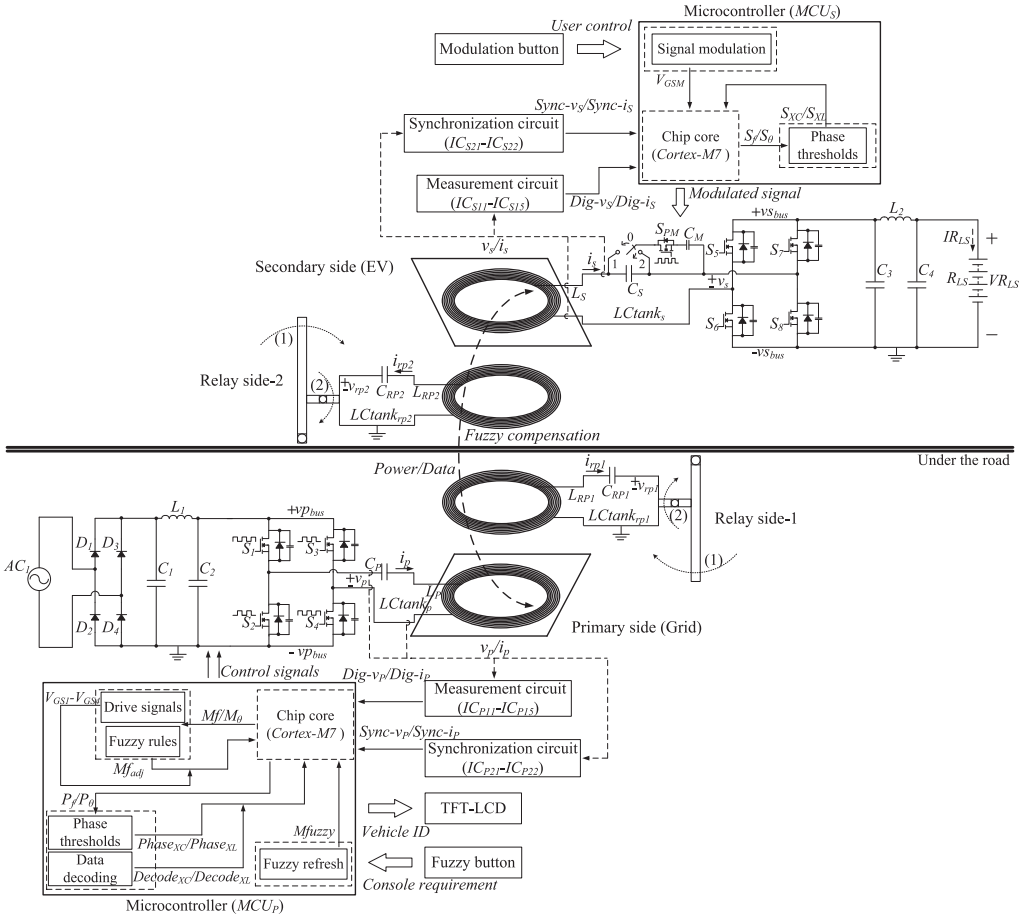

Fig. 3. Proposed WPT system for charging EVs with different chassis heights.

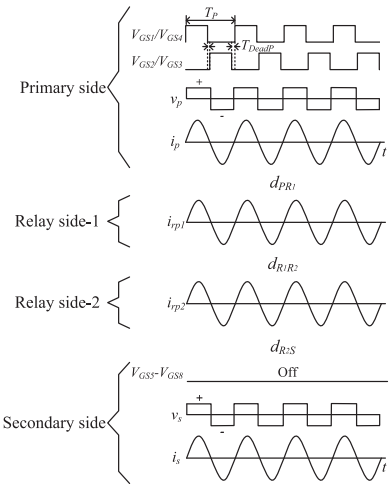

Fig. 4. Waveforms of the symmetrical full-bridge G_2V drive circuit.

gate signals of each group of power switches. The pulsewidth modulation signals for each group of power switches is set to 49% of the operating period T_P; the delay time $T_{\mathrm{Dead}P}$ is set to 1% to prevent the power switch signals of different groups from interleaving (see Fig. 4). The relationship between input and output voltages is expressed as follows:

$$v_p = \frac{4}{\pi} v_{p\mathrm{bus}} \tag{6}$$

where $v_{p\mathrm{bus}}$ is rectified voltage of ac1 and v_p is its peak value.

The $LC\mathrm{tank}_p$ derived through v_p/i_p on the primary side is coupled to $LC\mathrm{tank}_s$ on the secondary side to produce v_s/i_s. Then, v_s/i_s is converted to dc using the full-wave rectifier composed of S_5 to S_8 and is transmitted to the secondary side R_{LS}. $LC\mathrm{tank}_{rp1}$ and $LC\mathrm{tank}_{rp2}$ are generated by repeaters used in the power transmission process.

The low-pass filter on the primary side is composed of L_1, C_1, and C_2, and the low-pass filter on the secondary side is composed of L_2, C_3, and C_4. The filters are used to separately filter harmonic frequencies in order to avoid signal corruption from the grid side.

III. Design of Coil and Repeater

A. Mutual Inductance Changes Between Transmission Coils

The Biot–Savart law and Neumann's formula can be used to mathematically model the magnetic flux for two transmission coils with an air gap and horizontal misalignment (see Fig. 5). From which the mutual inductance can be derived as follows

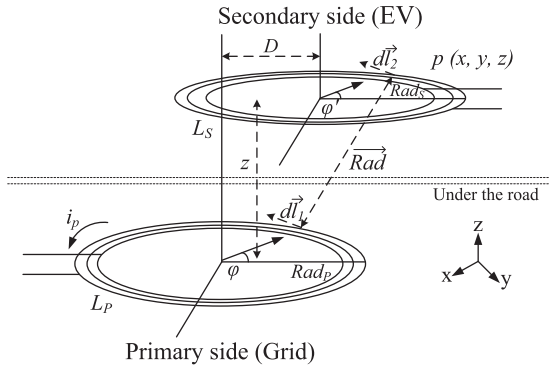

Fig. 5. Diagram of two misaligned transmission coils separated by an air gap.

[23]:

$$M_{PS} = \frac{\mu_0}{4\pi} \oint \oint \frac{d\vec{l_1} \cdot d\vec{l_2}}{\overrightarrow{Rad}} \tag{7}$$

where $d\vec{l_1}$ is the tangent vector of L_P, μ_0 is the vacuum permeability, and $\overrightarrow{Rad}$ is the distance vector between $d\vec{l_1}$ and $d\vec{l_2}$.

If the two transmission coils are not aligned or if the air-gap distance is not constant, $d\vec{l_1}$, $d\vec{l_2}$, and $\overrightarrow{Rad}$ can be rewritten, respectively, as

$$d\vec{l_1} \cdot d\vec{l_2} = Rad_P Rad_S \cos(\varphi - \varphi') d\varphi d\varphi' \tag{8}$$

and (9) shown at the bottom of this page, where $s = \sqrt{z^2 + D^2}$ with D and z being, respectively, the misalignment distance and the air-gap distance, φ is the angle corresponding to the L_P integral variable, and φ' is the angle corresponding to the L_S integral variable.

By substituting (8) and (9) into (7), one can calculate the mutual inductance as a function of the relative positions of the coils to each other. When D or z increases, M_{PS} decreases accordingly [25].

B. Mutual Inductance

The mutual inductance between the transmission coils is divided into mutual assistance and mutual cancellation [26]. They can be expressed as follows:

$$L_{\text{assistance}} = L_P + L_S + 2M_{PS} \tag{10}$$

$$L_{\text{cancellation}} = L_P + L_S - 2M_{PS}. \tag{11}$$

From the two equations, one can obtain the mutual inductance between two transmission coils as

$$M_{PS} = \frac{L_{\text{assistance}} - L_{\text{cancellation}}}{4}. \tag{12}$$

The proposed coil structures and the detailed experimental parameters are summarized in Table II.

TABLE II
EXPERIMENTAL COIL PARAMETERS FOR POWER AND DATA TRANSMISSION

Coil diameter	135 mm
Wire diameter	2.0 mm^2
Number of turns	14 turns
Wire type	*Litz-wire*
Soft ferrite	150 x 150 mm^2
Relative permeability of soft ferrite	1000
Self-inductance of coil	52.8 μH
Self-inductance of relay coil	30.2 μH
Coil resistance	0.1 Ω
Relay coil resistance	0.1 Ω

TABLE III
CALCULATED MUTUAL INDUCTANCE VALUES BETWEEN COILS

M (μH)		Coil misalignment (mm)					
		0	10	20	30	40	50
Air gap (mm)	0	25.40	23.93	20.48	16.15	12.35	8.68
	10	17.45	16.83	14.73	12.28	9.58	7.15
	20	12.33	11.73	10.88	9.53	7.38	5.90
	30	9.03	8.80	7.98	7.03	6.13	4.73
	40	6.65	6.38	6.00	5.48	4.88	3.80
	50	5.13	5.00	4.70	4.23	3.75	3.10

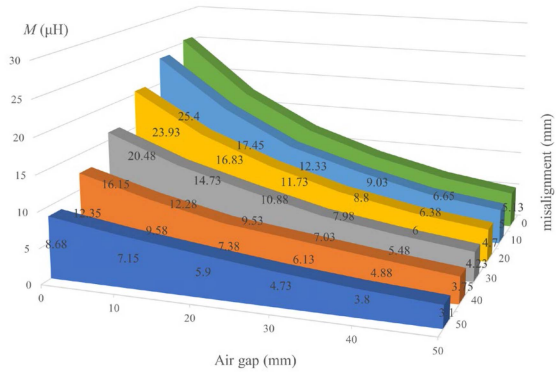

Fig. 6. Three-dimensional correlation diagram of mutual inductance versus air-gap distance and misalignment distance.

C. Performance Evaluation of Coils

Using (10) to (12) and coil parameters tabulated in Table I, one can calculate the mutual inductance between two coils at different values of D and z, as tabulated in Table III. As illustrated in Fig. 6, air-gap distance had a greater effect on mutual inductance than on coil misalignment.

It can be found from Figs. 5 and 7 that the change of the air gap has a greater impact on the mutual inductance and coupling coefficient. In addition, to comply with the *LC* coupling theory, the air gap between the coils must start from 30 mm ($Q > 10$). In practice, better flexibility and operability is achievable if the coupling coefficient K between both coils can be selected

$$\overrightarrow{Rad} = \sqrt{Rad_P^2 + Rad_S^2 + s^2 - 2Rad_P Rad_S \cos(\varphi - \varphi') + 2Rad_S D \cos\varphi' - 2Rad_P D \cos\varphi} \tag{9}$$

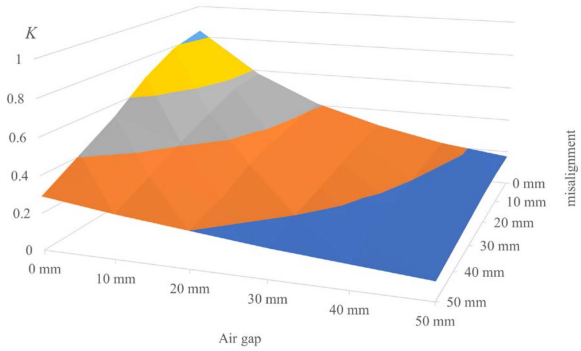

Fig. 7. Three-dimensional correlation diagram of coupling coefficient versus air-gap distance and misalignment distance.

TABLE IV
CALCULATED COUPLING COEFFICIENT BETWEEN COILS

K		Coil misalignment (mm)					
		0	10	20	30	40	50
Air gap (mm)	0	0.84	0.79	0.68	0.53	0.41	0.29
	10	0.58	0.56	0.49	0.41	0.32	0.24
	20	0.41	0.39	0.36	0.32	0.24	0.20
	30	0.30	0.29	0.26	0.23	0.20	0.16
	40	0.22	0.21	0.20	0.18	0.16	0.13
	50	0.17	0.17	0.16	0.14	0.12	0.10

appropriately [27], [28]. In the current case, the value is set below 0.3 using the relationship

$$K = \frac{M}{\sqrt{L_P L_S}}. \tag{13}$$

From (13) and Table III, the value of K is served as a function of air-gap and misalignment distance. The optimal air-gap distance between the two transmission coils was determined to be around 30 mm, as illustrated in Fig. 7 and Table IV.

IV. PROPOSED COMMUNICATION METHOD

A. Principle of Resonance

The principle of resonance is applied to realize data feedback. In Fig. 8(a), i_p cannot be transmitted to the secondary side without a mutually inducted wire loop on the secondary side, resulting in slow attenuation of i_p and longer free resonant time. In Fig. 8(b), i_p is transmitted to the secondary side using mutual inductance, resulting in a shorter time of free resonance. Accordingly, the load status can be detected before power transmission to activate data feedback.

B. Signal Modulation

The modulated electromagnetic wave is referenced to logic "0" or logic "1". Phase-shift keying (PSK) is a signal modulation method based on controlling the phase of a reference signal.

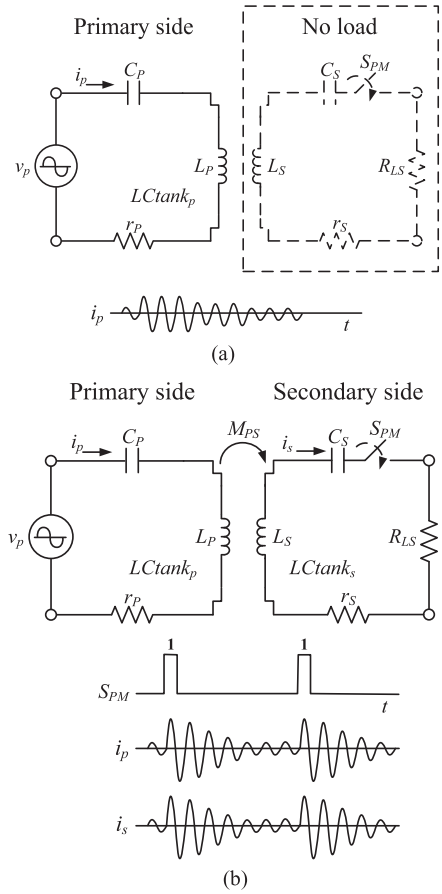

Fig. 8. Schematic diagrams of the resonance principle. (a) Free resonant current without mutual inductance. (b) Free resonant current with mutual inductance.

Multilevel PSK variants such as binary PSK, quadrature PSK, and 8PSK can be collectively referred to as M-ary PSK (MPSK), and the corresponding transmission formula can be expressed as follows:

$$S(t) = A_C \cos(2\pi f_C t + K_P M(t)) \tag{14}$$

where $S(t)$ represents the modulated signal, K_P represents the phase sensitivity of the modulated signal, f_C represents the modulation frequency, and $M(t)$ represents the signal to be transmitted. MPSK employs a set of M equal-energy signals to represent M equiprobable symbols. The signal set is analytically given by

$$S_i(t) = A_C \cos\left(2\pi f_C t + \frac{2\pi i}{M}\right), i = 1, 2 \cdots, M-1 \tag{15}$$

where i represents the modulated signal base.

MPSK has considerable advantages in modulation and demodulation. That is, it is able to transmit more data without an increase in an increase bandwidth. Also, it has excellent anti-interference properties and renders data recognition an intuitive process [29].

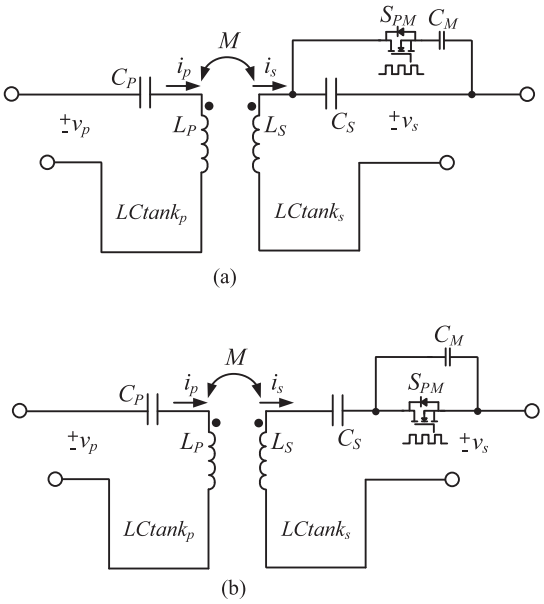

Fig. 9. Signal modulation of two different switching circuit architectures. (a) Using increasing capacitive reactance (Mode 1). (b) Using decreasing capacitive reactance (Mode 2).

C. Communication of Impedance Changes

Fig. 9 illustrates the proposed data modulation circuit with two resonance-based working modes. These two modes use either reactive capacitance or inductive capacitance to realize MPSK modulation. Fig. 10 shows the modulation waveforms.

1) Mode 1: When the microcontroller units (MCU_S) turn on the switch S_{PM}, the capacitive reactance of the secondary side increases, and the phase of i_s changes accordingly. This causes the phase of i_p to lead the phase of v_p. MCU_P uses the difference in phase angle between the signals *Sync-*v_P and *Sync-*i_P to create the signal Phase_{XC}. The signal Decode_{XC} is then either "0" or "1," according to the value of Modulation_{XC}

$$\text{Modulation}_{XC} = \left\{ \left[\frac{\left(\theta i_P / T i_P\right) + \left(T'_{XC} / T_{XC}\right)}{2} \right] \cdot 360 \right\}. \tag{16}$$

When Modulation_{XC} is greater than zero, Decode_{XC} is "1" (and vice versa). When Modulation_{XC} is zero, it is compared with the result of the previous cycle for preliminary error detection.

2) Mode 2: When S_{PM} is turned ON, the capacitive reactance of the secondary side decreases, and the phase of i_s changes accordingly. This causes the phase of i_p to lag the phase of v_p. Phase_{XL} is the difference in phase angles between *Sync-*v_P and *Sync-*i_P. When Modulation_{XL} meets the following condition; Decode_{XL} is "1" (and vice versa)

$$\text{Modulation}_{XL} = \left\{ \left[\frac{\left(\theta v_P / T v_P\right) + \left(T'_{XL} / T_{XL}\right)}{2} \right] \cdot 360 \right\} \geq 40. \tag{17}$$

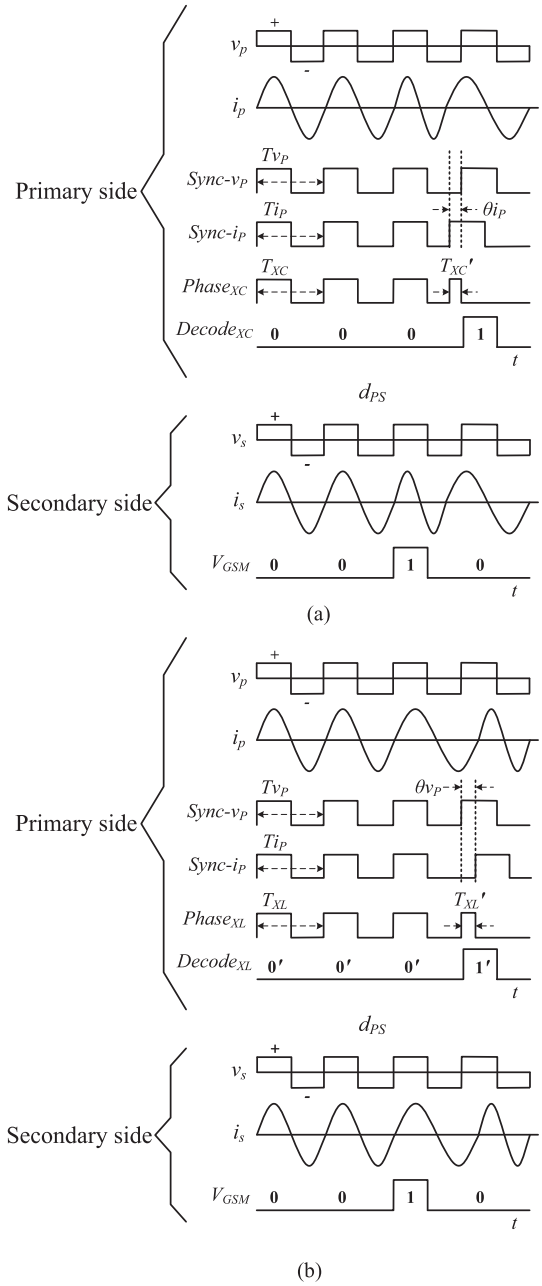

Fig. 10. Diagrams of communication waveforms in both modulation modes. (a) Increasing capacitive reactance modulation (Mode 1). (b) Decreasing capacitive reactance modulation (Mode 2).

D. Fuzzy Compensation

Mutual inductance and phase angle (θ) are central to our WPT system. According to SAE TIR J2954, M and θ are influential and must be explored. Fig. 11 shows that when the transmission coils are misaligned, the mutual inductance and phase angle would change, leading to deteriorating data communication quality. Therefore, a compensation mechanism was incorporated into our WPT system to address this problem.

Intelligent control based on the neural networks [30] or fuzzy logic theory [31] has been widely used in various fields of the modern power systems. It is useful to deal with situations when

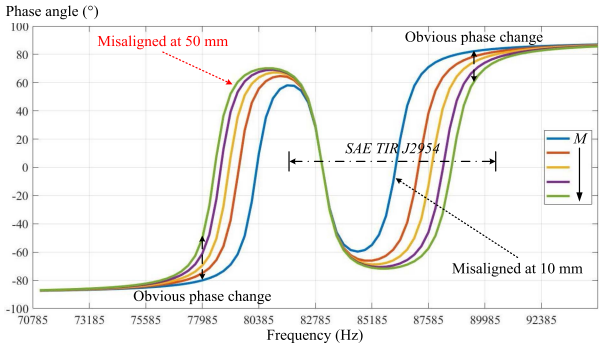

Fig. 11. Relationship between phase angle and frequency as a function of mutual inductance.

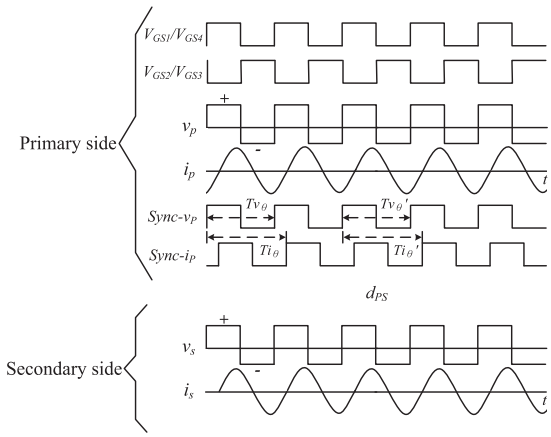

Fig. 12. Waveforms sent to MCU$_P$ for phase calculation.

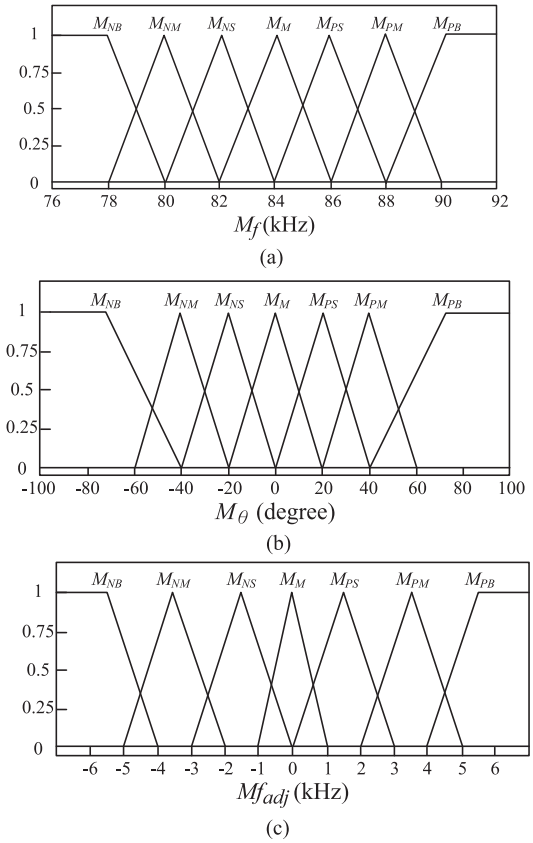

Fig. 13. Diagrams of membership functions for misaligned coils. (a) Membership functions of the fuzzified M_f. (b) Membership function of the fuzzified M_θ. (c) Membership functions of the fuzzified Mf_{adj}.

there is no way to establish a clear I/O relationship between the two inputs and output. A fuzzy compensation scheme is proposed here by considering phase angle and operating frequency for compensation of coil misalignment.

As displayed in Fig. 11, the correlation between the phase angle and mutual inductance would change when the operating frequency is in between 76 and 92 kHz. Therefore, *Sync-*v_P and *Sync-*i_P received by MCU$_P$ are used to calculate the voltage-current phase difference variable M_θ ($M_\theta \geq 0$ meant v_p leads i_p; otherwise, i_p leads v_p) and MCU$_P$ adjusts for the optimal operating frequency to counter excessive phase change, in accordance with SAE TIR J2954. The waveforms used for M_θ calculation are shown in Fig. 12. M_θ can be calculated as follows:

$$M_\theta = \left[\frac{(Ti_\theta - Tv_\theta) + (Ti'_\theta - Tv'_\theta)}{Tv_\theta + Tv'_\theta}\right] \cdot 360 \qquad (18)$$

where Ti_θ and Ti'_θ are the cycle time differences between *Sync-*v_P and *Sync-*i_P.

The proposed compensation strategy is based on fuzzy logic control to ensure optimal power transmission and data feedback when two coils are misaligned. Fig. 13 shows the defined membership functions of two inputs, i.e., the current operating frequency M_f and the phase difference variable M_θ and output, i.e., the incremental operating frequency Mf_{adj}. They divide the current frequencies M_f and M_θ into seven fuzzy subsets of M_{NB} to M_{PB}. Using triangular membership functions is easily conducive to real-time control. The defuzzification strategy is the center-of-gravity method expressed as follows:

$$y^0 = \frac{\sum_{i=1}^{l} \mu_{\tilde{B}}(y_i) \cdot y_i}{\sum_{i=1}^{l} \mu_{\tilde{B}}(y_i)} \qquad (19)$$

where l represents the quantized number of the output fuzzy variable y, y^0 represents the unambiguous output after defuzzification, y_i represents the ith quantized value of y, and $\mu_{\tilde{B}}(y_i)$ represents the attribution degree of y_i in the fuzzy set B.

To comply with the SAE standard, the rule table cannot be fully symmetric if the phase difference between the induction voltage and current is set to zero and the output frequency is set to the range between 81.38 and 90 kHz. The established fuzzy control rules are summarized in Table V. Fig. 14 illustrates the graphical relationship between (M_f, M_θ) and Mf_{adj}. It can be observed that the inferred frequency adjustment would be significantly react when (M_f, M_θ) is deviated from the nominal setting at (85.7 kHz, 0°).

TABLE V
FUZZY RULE BASE FOR COIL MISALIGNMENT COMPENSATION

Mf_{adj} (kHz)		Mf (kHz)						
		M_{NB}	M_{NM}	M_{NS}	M_M	M_{PS}	M_{PM}	M_{PB}
M_θ (degree)	M_{NB}	M_{PB}	M_{PM}	M_{PS}	M_{PS}	M_{PS}	M_{PS}	M_M
	M_{NM}	M_{PB}	M_{PM}	M_{PS}	M_{PS}	M_{PS}	M_M	M_{NS}
	M_{NS}	M_{PB}	M_{PS}	M_{PS}	M_M	M_{PS}	M_M	M_{NS}
	M_M	M_{PM}	M_{PS}	M_M	M_M	M_M	M_M	M_{NS}
	M_{PS}	M_{PM}	M_{PS}	M_M	M_M	M_M	M_{NS}	M_{NM}
	M_{PM}	M_{PS}	M_M	M_M	M_{NS}	M_{NS}	M_{NS}	M_{NB}
	M_{PB}	M_{PS}	M_M	M_M	M_{NS}	M_{NS}	M_{NM}	M_{NB}

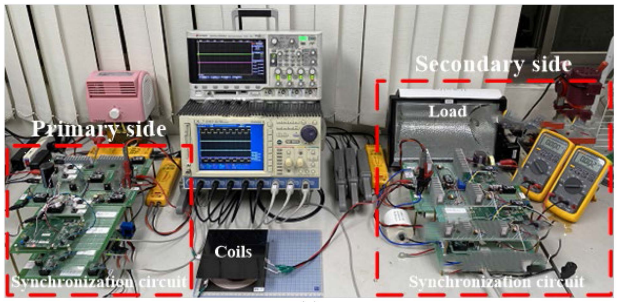

(a)

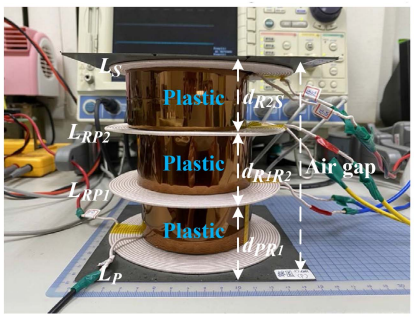

(b)

Fig. 14. Architecture for system performance verification. (a) Hardware installation of the experimental WPT system (b) The WPT system uses a two-repeater architecture (the allowable air-gap distance is boosted to 120 mm).

V. VERIFICATION AND ANALYSIS

The main circuit includes a resonant inverter, resonant repeaters, a full-wave rectifier, a modulation circuit, measurement circuits, and synchronization circuits. The microcontroller handles power drive, fuzzy compensation, signal modulation, and data encoding and decoding. The specifications and key parameters of our WPT system are summarized in Table VI.

The MOSFETs used in the resonant inverter, consisting of the third-generation wide-band-gap semiconductor silicon carbide, have higher efficiency, power density, and switching frequency than silicon MOSFETs. Therefore, they can work to comply with the frequency specification of SAE TIR *J2954*. In the analysis, a 1 kW halogen searchlight was used as a pure resistive load. This was use to prevent the generation of extra inductance or capacitance that could distort the verification results. Fig. 14 depicts photos of the hardware setup, and Fig. 15 displays the system operational flowchart.

TABLE VI
SPECIFICATIONS OF THE WPT SYSTEM AND KEY COMPONENTS

Resonance compensation	Series compensation (*S-S*)
Nomial system frequency	83 kHz
Input power	5 kW
Rated output power	800 W
MOSFET_V_{DS}/$I_{D\,(25°C)}$ (S_1-S_8/S_{PM})	1200 V/36 A
Resonant capacitor (C_P/C_S)	0.07 μF
Modulation capacitor (C_M)	0.07 μF
Repeater capacitor (C_{RP1}/C_{RP2})	0.07 μF
Load resistance (R_{LS})	5.5 Ω
Initial air gap distance	40 mm
Distance between the resonators	40 mm

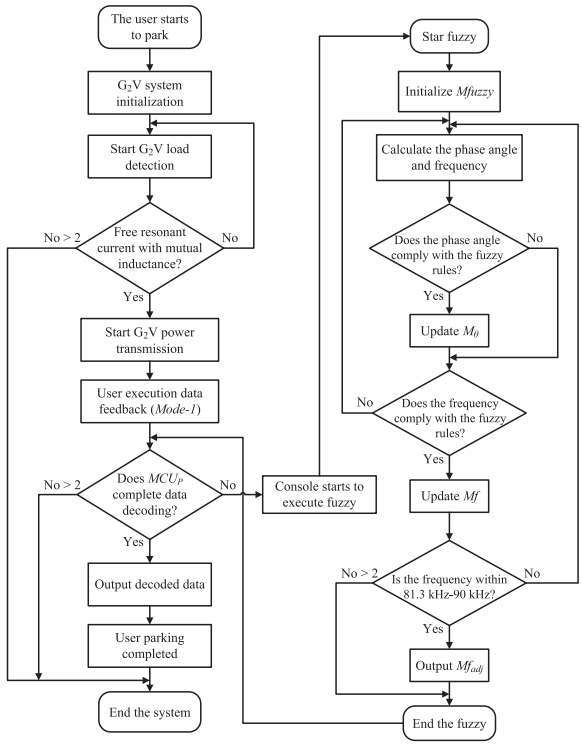

Fig. 15. G_2V process for simultaneous power and data transmission.

VI. EXPERIMENTAL VERIFICATION

A. G_2V Wireless Power Transmission

Fig. 16 illustrates the waveforms of our WPT system using a two-coil (primary and secondary coils) architecture. In this figure, Channel 1 indicates the driving signal waveform of S_1 (V_{GS1}); Channels 2 and 3 indicate the voltage v_p (in green) and current i_p (in purple) waveforms of $LC\text{tank}_p$ (v_p/i_p), respectively; and Channels 4 and 5 indicate the voltage v_s (in light blue) and current i_s (in red) waveforms of $LC\text{tank}_s$ (v_s/i_s), respectively.

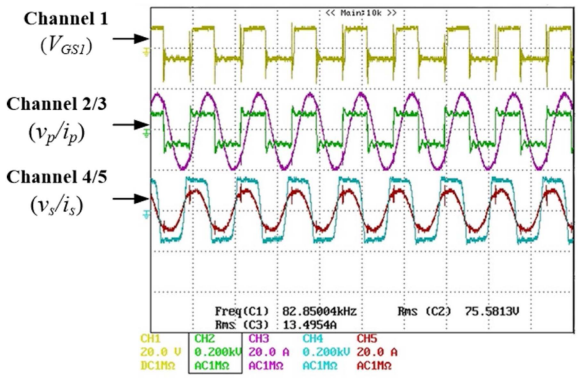

Fig. 16. System waveforms of the two-coil architecture.

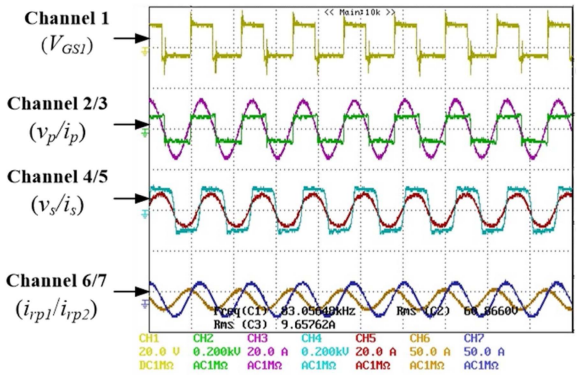

Fig. 17. System waveforms of the two-repeater architecture.

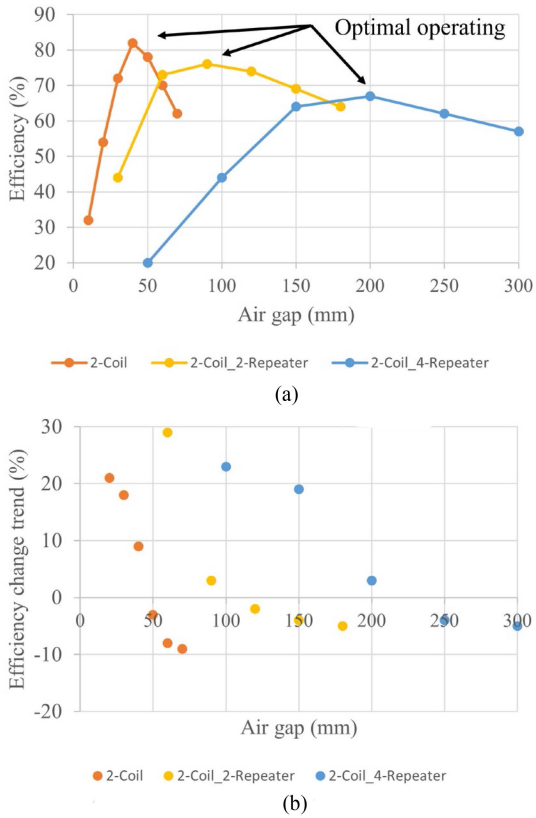

Fig. 18. Analysis of PTE of various WPT architectures at different air-gap distances. (a) Efficiency versus air-gap distance. (b) Change in efficiency versus air-gap distance.

These waveforms demonstrate the operational stability of the system.

Fig. 17 shows the waveforms of our WPT system using a two-repeater (four-coil) architecture. In this figure, Channels 6 and 7 indicate the current waveforms on the relay side (i_{rp1}/i_{rp2}). These waveforms confirm the stability of the system.

B. Air-Gap Distance and PTE

The experimental relationship between PTE and air-gap distance for different architectures is illustrated in Fig. 18. It is determined that 1) the optimal operating air-gap distance for the two-coil architecture was between 35 and 45 mm, which is consistent with our findings in Section III; 2) the use of repeaters could effectively increase the power transmission distance and efficiency; and 3) the use of more repeaters could mitigate PTE decay with increasing air-gap distance.

Fig. 18 has shown power transfer efficiency versus no repeater, two repeaters, and four repeaters. The range of optimal operating air gap is wider when using more repeaters. However, it also shows that the overall power transfer efficiency decreases with the increasing number of repeaters, but the allowable air gap between coils increases with the number of repeaters. The fact is understandable because of the mutual inductance would be decreasing with more repeaters involved. Therefore, there is a compromise to be considered when adopting an appropriate number of repeaters to extend power transfer distance.

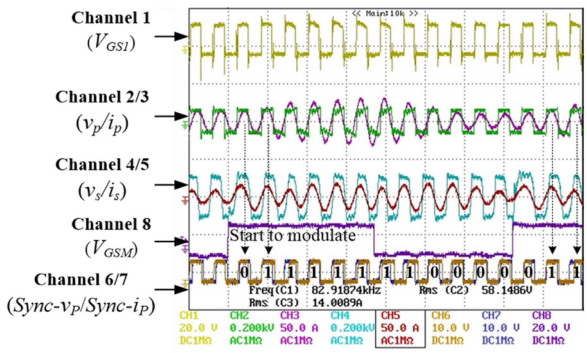

Fig. 19. Simultaneous power transmission and data feedback waveforms of the two-coil architecture (mode 1).

C. Simultaneous G_2V Power Transmission and Data Feedback

The power transmission and data feedback waveforms derived for the two-coil architecture in Modes 1 and 2 are presented in Figs. 19 and 20, respectively, where Channels 6 and 7 indicate the waveforms of the synchronous voltage and current signals (Sync-v_P/Sync-i_P), respectively, and Channel 8 indicates the modulated signal of S_{PM} (V_{GSM}). It is observed that the primary

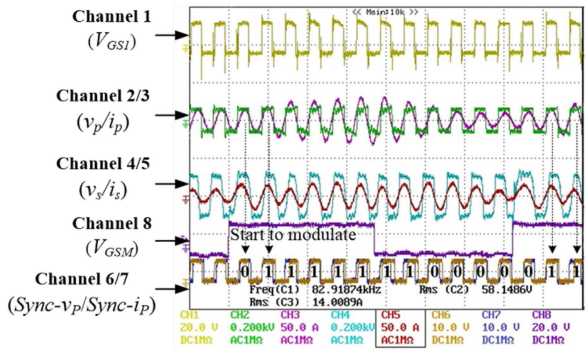

Fig. 20. Simultaneous power transmission and data feedback waveforms of the two-coil architecture (mode 2).

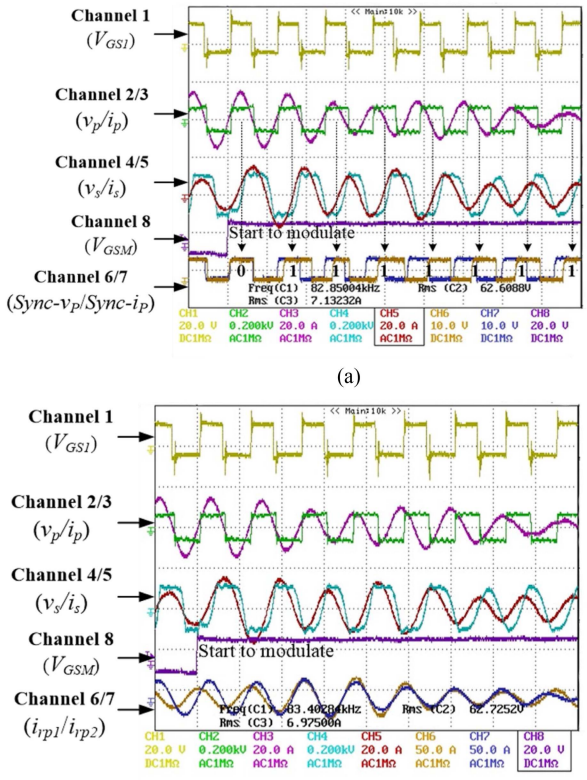

Fig. 21. Data feedback and power transmission waveforms of the two-repeater architecture (mode 1). (a) Data decoding waveforms. (b) Current waveforms on the relay side.

side correctly decoded data sent back from the secondary side in both modes.

The power transmission and data feedback waveforms derived for the two-repeater architecture are displayed in Fig. 21. As illustrated in Fig. 21(a), although the system architecture was changed, the primary side still correctly decoded the data sent from the secondary side in Mode 1. In Fig. 21(b), Channels 6 and 7 indicate the current waveforms on the relay side (i_{rp1}/i_{rp2}). These results indicate that the two-repeater architecture could enable the execution of power transmission and data feedback simultaneously.

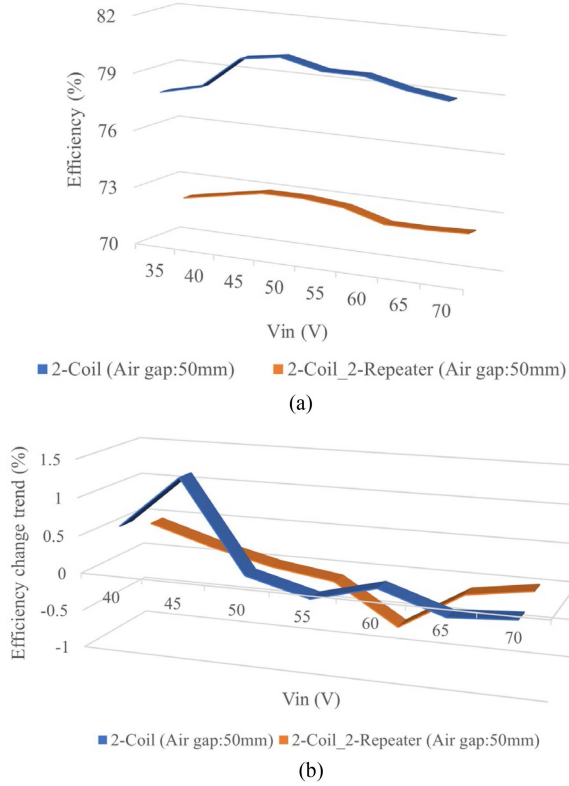

Fig. 22. Analysis of MPSK and voltage changes of various WPT architectures (mode 1). (a) PTE versus input voltage. (b) Change in PTE versus input voltage.

D. MPSK and PTE

Our design uses two cycles of transmission time to decode 1 bit. Therefore, the system bit rate is at least 41.5 kb/s. To explore the effect of MPSK on PTE, the signal modulation at different input voltages was verified. The statistical results are illustrated in Fig. 22, revealing that the system efficiency could be maintained above 70% for both WPT system architectures using signal modulation [see Fig. 22(a)] and that the PTE only fluctuated by at most 2% at different input voltages [see Fig. 22(b)].

E. Simultaneous G_2V Power and Data Transmission With Fuzzy Compensation

Fig. 23(a) illustrates the system waveforms derived when the two-coil architecture was misaligned at 40 mm. Channel 1 shows the drive signal waveform of S_1. Channels 2 and 3 display, respectively, the voltage and current waveforms of $LC\text{tank}_p$. Channels 4 and 5 display, respectively, the voltage and current waveforms of $LC\text{tank}_s$. Channels 6 and 7 display, respectively, the waveforms of the synchronous voltage and current signals. Channel 8 is the modulated signal of S_{PM}. When two coils were misaligned, the original phase angle of the system changed (as shown in Channels 2/3), leading to data communication failure.

To resolve the problem, fuzzy compensation was applied by following the flowchart illustrated in Fig. 15. As shown in Fig. 23(b), the executed fuzzy compensation process effectively

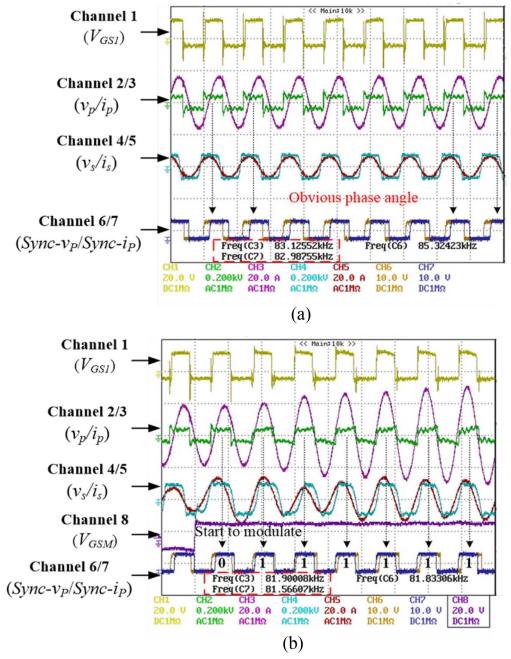

Fig. 23. Effect of fuzzy compensation on simultaneous power and data transmission of the two-coil architecture. (a) Phase changes caused by coil misalignment ($D = 40$ mm). (b) Successfully decoding the feedback data through fuzzy compensation (Mode 1).

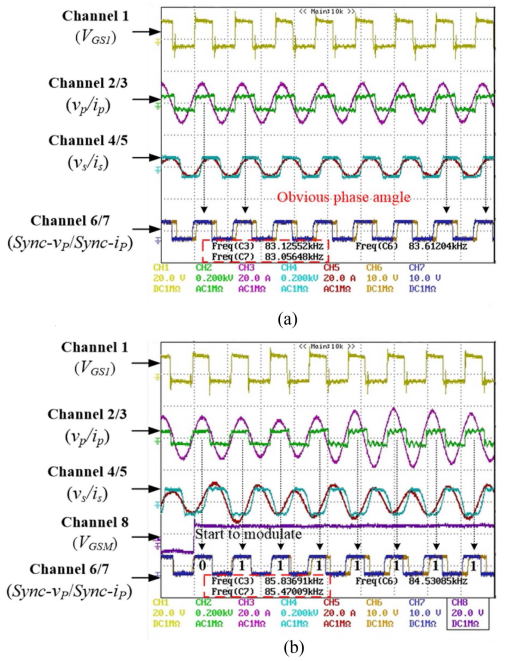

Fig. 24. Effect of fuzzy compensation on simultaneous power and data transmission of the two-repeater architecture. (a) Phase changes caused by coil misalignment ($D = 20$ mm). (b) Successfully decoding the feedback data through fuzzy compensation 12 (Mode 1).

reduced the phase angle by adjusting M_θ and M_f, and adjusting Mf_{adj} maintained the operational frequency between 81.38 and 90 kHz. In which, feedback data sent from the secondary side were decoded by MCU_P.

The preceding results demonstrate the viability of the system for low-chassis EVs. Accordingly, to simulate high-chassis EVs, the stacked-repeater architecture was considered. Fig. 24 displays the results obtained for simultaneous power and data transmission after compensation, demonstrating the effectiveness of the fuzzy compensator. As of the results of Fig. 23, the data are decoded correctly, as shown in Channel 6/7 of Fig. 24(b).

The correlation of M_θ, M_f, and Mf_{adj} to coil misalignment is, thus, approved and verified.

F. Phase Angle and PTE

The experimental relationships between phase angle and PTE for all tested architectures are displayed in Figs. 25–27. It is observed that 1) fuzzy compensation reduced the phase difference, thus improving PTE, regardless of coil alignment; 2) fuzzy compensation corrected the phase angles of the systems, especially those of the stacked-repeater architectures for longer power and data transmission distances; 3) our system verification process could detect coil misalignment; and 4) undercoupling and efficiency drop became significant when the coil misalignment distance increased to 50 mm.

The experimental result shows difference between with and without fuzzy compensation. It is clearly that for 1) the two signal modulation methods used did not significantly affect frequency bandwidth but greatly increased system availability for data encoding and decoding and 2) fuzzy compensation

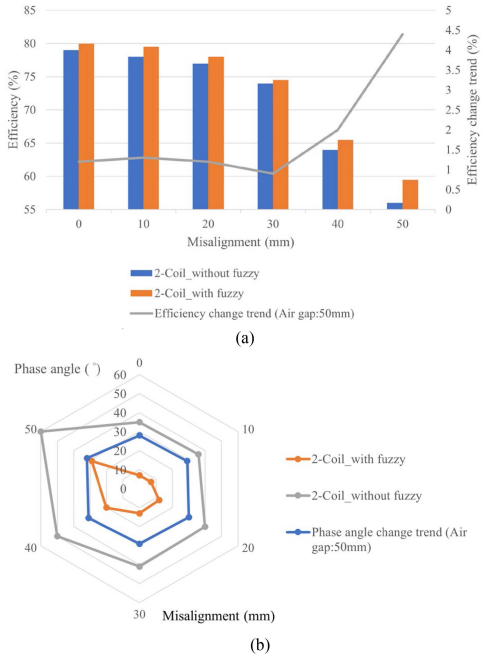

Fig. 25. Analysis of the two-coil architecture with coil misalignment. (a) Effect of fuzzy compensation on PTE. (b) Correlation between fuzzy compensation and phase angle.

effectively improved PTE for horizontal coil misalignment and involvement of the repeaters increase PTE for vertical air gap. A combination of both designs would be useful to resolve the issue of vehicle parking deviation.

It should finally be mentioned that our proposed approach is universal, however, in practical applications, the coils chosen

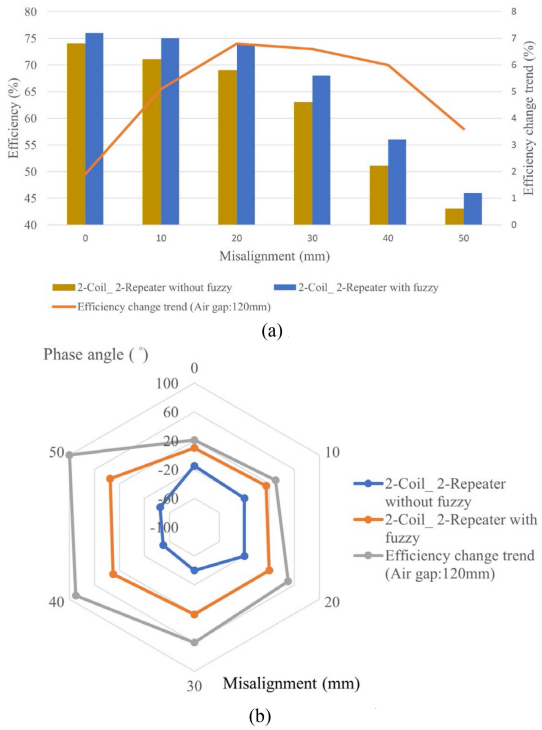

Fig. 26. Analysis of the two-repeater architecture with coil misalignment. (a) Effect of fuzzy compensation on PTE. (b) Correlation between fuzzy compensation and phase angle

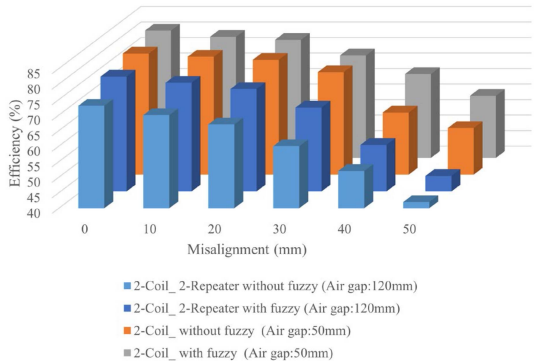

Fig. 27. Comparison of PTE for various architectures with misaligned two coils.

should still be tuned according to the operating frequency, power to be transferred and characteristics of payload.

Sampled video clips of real-world experimental demonstrations of the prototype WTP system can be found in [32].

VII. Conclusion

This article has successfully demonstrated an adaptive WPT system with relay power transmission and magnetic field communication that complies with SAE TIR J2954. Using additional repeaters is proved to effectively overcome the difficulty of charging EVs with different chassis heights, thus enhancing the applicability of our WPT system. Data transmission using magnetic field avoids pairing problems and electromagnetic interference, and our design does not require additional RF devices for this purpose. Moreover, our encoding and decoding method can measure the vehicle parking deviation over the charging system without using an extra sensing mechanism. Fuzzy compensation can ensure robust system operation for both transmission types. Finally, our symmetrical design structure can potentially allow bidirectional power and data transmission (G_2V and V_2G) in future studies.

The following observations were made through our verification analysis: 1) the two signal modulation methods used did not significantly affect frequency bandwidth but greatly increased system availability for data encoding and decoding; and 2) fuzzy compensation improved PTE for longer-distance transmission, which resolved problems caused by vehicle parking deviation.

References

[1] P. K. Chittoor, B. Chokkalingam, and L. Mihet-Popa, "A review on UAV wireless charging: Fundamentals, applications, charging techniques and standards," *IEEE Access*, vol. 9, pp. 69235–69266, 2021.

[2] G. R. Kalra, D. J. Thrimawithana, B. S. Riar, C.-Y. Huang, and M. Neuburger, "A novel boost active bridge-based inductive power transfer system," *IEEE Trans. Ind. Electron.*, vol. 67, no. 2, pp. 1103–1112, Feb. 2020.

[3] M. Tian, W. Jiao, and J. Liu, "The charging strategy of mobile charging vehicles in wireless rechargeable sensor networks with heterogeneous sensors," *IEEE Access*, vol. 8, pp. 73096–73110, 2020.

[4] A. N. Azad, A. Echols, V. A. Kulyukin, R. Zane, and Z. Pantic, "Analysis, optimization, and demonstration of a vehicular detection system intended for dynamic wireless charging applications," *IEEE Trans. Transp. Electrific.*, vol. 5, no. 1, pp. 147–161, Mar. 2019.

[5] M. J. Karimi, A. Schmid, and C. Dehollain, "Wireless power and data transmission for implanted devices via inductive links: A systematic review," *IEEE Sens. J.*, vol. 21, no. 6, pp. 7145–7161, Mar. 2021.

[6] Z. Zhang, H. Pang, A. Georgiadisand, and C. Cecati, "Wireless power transfer—An overview," *IEEE Trans. Ind. Electron.*, vol. 66, no. 2, pp. 1044–1058, Feb. 2019.

[7] M. Dionigi, A. Costanzo, F. Mastri, and M. Mongiardo, *Magnetic Resonant Wireless Power Transfer*. Berlin, Germany: Research Gate, 2012, pp. 157–197.

[8] N. Shinohara, Y. Kubo, and H. Tonomura, "Wireless charging for electric vehicle with microwaves," in *Proc. Int. Electric Drives Prod. Conf.*, 2013, pp. 1–4, doi: 10.1109/EDPC.2013.6689750.

[9] "Wireless power transfer for light-duty plug-in/electric vehicles and alignment methodology," J2954_201904, Ground Vehicle Standard, Glenview, IL, United States, 2020.

[10] L. Zhao, D. J. Thrimawithana, U. K. Madawala, and A. P. Hu, "A push–pull parallel resonant converter-based bidirectional IPT system," *IEEE Trans. Power Electron.*, vol. 35, no. 3, pp. 2659–2667, Mar. 2020.

[11] A. A. S. Mohamed and O. Mohammed, "Physics-based co-simulation platform with analytical and experimental verification for bidirectional IPT system in EV applications," *IEEE Trans. Veh. Technol.*, vol. 67, no. 1, pp. 275–284, Jan. 2018.

[12] F. Liu, K. Li, K. Chen, and Z. Zhao, "A phase synchronization technique based on perturbation and observation for bidirectional wireless power transfer system," *IEEE J. Emerg. Sel. Topics Power Electron.*, vol. 8, no. 2, pp. 1287–1297, Jun. 2020.

[13] Y. Liu, U. K. Madawala, R. Mai, and Z. He, "Primary-side parameter estimation method for bidirectional inductive power transfer systems," *IEEE Trans. Power Electron.*, vol. 36, no. 1, pp. 68–72, Jan. 2021.

[14] S. Ghimirey, C. Roy, and A. Sengupta, "Wireless electricity transfer using inductive power transfer system," in *Advanced Computational Paradigms and Hybrid Intelligent Computing*. Berlin, Germany: Springer-Verlag, 2022, doi: 10.1007/978-981-16-4369-9_32.

[15] T. S. Pham et al., "Optimal frequency for magnetic resonant wireless power transfer in conducting medium," *Sci. Rep.*, vol. 11, 2021, Art. no. 18690.

[16] J. S. Choi, S. Y. Jeong, B. G. Choi, S.-T. Ryu, C. T. Rim, and Y. S. Kim, "Air-gap-insensitive IPT pad with ferromagnetic and conductive plates," *IEEE Trans. Power Electron.*, vol. 35, no. 8, pp. 7863–7872, Aug. 2020.

[17] J. Wu, C. Zhao, Z. Lin, J. Du, Y. Hu, and X. He, "Wireless power and data transfer via a common inductive link using frequency division multiplexing," *IEEE Trans. Ind. Electron.*, vol. 62, no. 12, pp. 7810–7820, Dec. 2015.

[18] J. Lee, K. Lee, and D.-H. Cho, "Stability improvement of transmission efficiency based on a relay resonator in a wireless power transfer system," *IEEE Trans. Power Electron.*, vol. 32, no. 5, pp. 3297–3300, May 2017.
[19] F. Wen, X. Chu, Q. Li, R. Li, L. Liu, and F. Jing, "Optimization on three-coil long-range and dimension-asymmetric wireless power transfer system," *IEEE Trans. Electromagn. Compat.*, vol. 62, no. 5, pp. 1859–1868, Oct. 2020.
[20] P. K. S. Jayathurathnage, A. Alphones, and D. M. Vilathgamuwa, "Optimization of a wireless power transfer system with a repeater against load variations," *IEEE Trans. Ind. Electron.*, vol. 64, no. 10, pp. 7800–7809, Oct. 2017.
[21] L. Qian, M. Chen, K. Cui, G. Shi, J. Wang, and Y. Xia, "Modeling of mutual inductance between two misalignment planar coils in wireless power transfer," *IEEE Microw. Wireless Compon. Lett.*, vol. 30, no. 8, pp. 814–817, Aug. 2020.
[22] Y. Chen, R. Mai, Y. Zhang, M. Li, and Z. He, "Improving misalignment tolerance for IPT system using a third-coil," *IEEE Trans. Power Electron.*, vol. 34, no. 4, pp. 3009–3013, Apr. 2019.
[23] J.-J. Kao, C.-L. Lin, Y.-C. Liu, C.-C. Huang, and H.-S. Jian, "Adaptive bidirectional inductive power and data transmission system," *IEEE Trans. Power Electron.*, vol. 36, no. 7, pp. 7550–7563, Jul. 2021.
[24] C. Zhang, D. Lin, N. Tang, and S. Y. R. Hui, "A novel electric insulation string structure with high-voltage insulation and wireless power transfer capabilities," *IEEE Trans. Power Electron.*, vol. 33, no. 1, pp. 87–96, Jan. 2018.
[25] Y. Gao, C. Duan, A. A. Oliveira, A. Ginart, K. B. Farley, and Z. T. H. Tse, "3-D coil positioning based on magnetic sensing for wireless EV charging," *IEEE Trans. Transp. Electrific.*, vol. 3, no. 3, pp. 578–588, Sep. 2017.
[26] C. Wang, "Design of a spiral coils platform for inductive contactless power transfer," M.S. thesis, Nat. Sun Yat-sen Univ., Kaohsiung, Taiwan, 2017.
[27] Z. Yan, Y. Li, C. Zhang, and Q. Yang, "Influence factors analysis and improvement method on efficiency of wireless power transfer via coupled magnetic resonance," *IEEE Trans. Magn.*, vol. 50, no. 4, Apr. 2014, Art. no. 4004204.
[28] F. Corti, F. Grasso, A. Reatti, A. Ayachit, D. K. Saini, and M. K. Kazimierczuk, "Design of class-E ZVS inverter with loosely-coupled transformer at fixed coupling coefficient," in *Proc. Ann. Conf. IEEE Ind. Electron. Soc.*, 2016, pp. 5627–5632.
[29] G. Jajoo, Y. Kumar, and S. K. Yadav, "Blind signal PSK/QAM recognition using clustering analysis of constellation signature in flat fading channel," *IEEE Commun. Lett.*, vol. 23, no. 10, pp. 1853–1856, Oct. 2019.
[30] H. Hamdi, C. B. Regaya, and A. Zaafouri, "A sliding-neural network control of induction-motor-pump supplied by photovoltaic generator," *Protection Control Modern Power Syst.*, vol. 5, no. 1, pp. 1–17, 2020.
[31] C. B. Regaya, F. Farhani, A. Zaafouri, and A. Chaari, "Proportional-integral field oriented control of induction motor with fuzzy logic gains adaptation," *Int. J. Control Syst. Robot.*, vol. 4, pp. 115–123, 2019.
[32] "Demonstrative video." Accessed: Dec. 26, 2021. [Online]. Available: https://youtu.be/O-AFv7gg_Dw

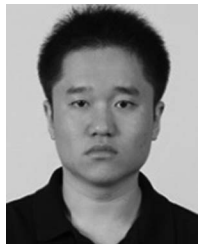

Jia-Jing Kao was born in Taichung, Taiwan, in 1983. He received the M.S. degree from National Chin Yi University of Technology, Taichung, Taiwan, in 2016, and the Ph.D. degree from the National Chung Hsing University, Taichung, Taiwan, in 2022, both in electrical engineering.

His research interests include power electronics and communication design with applications.

Chun-Liang Lin (Senior Member, IEEE) was born in Tainan, Taiwan, in 1958. He received the Ph.D. degree in aeronautical and astronautical engineering from the National Cheng Kung University, Tainan, Taiwan, in 1991.

He was an Associate Professor and Professor with the Department of Automatic Control Engineering, Feng Chia University, Taichung, Taiwan, from 1995 to 2003. He is currently a Chair Professor with the Department of Electrical Engineering, National Chung Hsing University, Taichung, Taiwan. His research interests include guidance and control, intelligent control, network control, and robust control.

Jamie Yang was born in Iowa, USA, in 1993. He is currently working toward the M.S. degree in the direction of wireless power transfer with the Department of Electrical Engineering, National Chung Hsing University, Taichung, Taiwan.

His research interests include power electronics with applications.